PNAS RESEARCH ARTICLE | NEUROSCIENCE

A fluorescent nanosensor paint detects dopamine release at axonal varicosities with high spatiotemporal resolution

Sofia Elizarova[a,b,c], Abed Alrahman Chouaib[d], Ali Shaib[a,e], Björn Hill[f], Florian Mann[g], Nils Brose[a], Sebastian Kruss[f,g,h,1], and James A. Daniel[a,1]

Edited by Robert Edwards, University of California, San Francisco, CA; received March 4, 2022; accepted April 8, 2022

The neurotransmitter dopamine (DA) controls multiple behaviors and is perturbed in several major brain diseases. DA is released from large populations of specialized structures called axon varicosities. Determining the DA release mechanisms at such varicosities is essential for a detailed understanding of DA biology and pathobiology but has been limited by the low spatial resolution of DA detection methods. We used a near-infrared fluorescent DA nanosensor paint, adsorbed nanosensors detecting release of dopamine (AndromeDA), to detect DA secretion from cultured murine dopaminergic neurons with high spatial and temporal resolution. We found that AndromeDA detects discrete DA release events and extracellular DA diffusion and observed that DA release varies across varicosities. To systematically detect DA release hotspots, we developed a machine learning–based analysis tool. AndromeDA permitted the simultaneous visualization of DA release for up to 100 dopaminergic varicosities, showing that DA release hotspots are heterogeneous and occur at only ∼17% of all varicosities, indicating that many varicosities are functionally silent. Using AndromeDA, we determined that DA release requires Munc13-type vesicle priming proteins, validating the utility of AndromeDA as a tool to study the molecular and cellular mechanism of DA secretion.

dopamine | neurotransmission | chemical signaling | sensors | imaging

Significance

The neurotransmitter dopamine controls normal behavior and dopaminergic dysfunction is prevalent in multiple brain diseases. To reach a detailed understanding of how dopamine release and signaling are regulated at the subcellular level, we developed a near infrared fluorescent dopamine nanosensor 'paint' (AndromeDA) to directly image dopamine release and its spatiotemporal characteristics. With AndromeDA, we can ascribe discrete DA release events to defined axonal varicosities, directly assess the heterogeneity of DA release events across such release sites, and determine the molecular components of the DA release machinery. AndromeDA thus provides a new method for gaining fundamental insights into the core mechanisms of dopamine release, which with greatly benefit our knowledge of dopamine biology and pathobiology.

The modulatory neurotransmitter dopamine (DA) controls a range of brain processes, from motor function to reward and motivation (1, 2). Aberrant DA signaling, on the other hand, is causally involved in multiple brain disorders, including Parkinson's disease, schizophrenia, and addiction (3–5). Despite this eclectic functional relevance, little is known about the molecular and cellular mechanisms that mediate and control DA release.

Fast neurotransmitters, such as glutamate, operate with high spatial and temporal accuracy. Our understanding of fast neurotransmission has been greatly advanced through methods that allow the study of fast neurotransmission with high precision, including imaging of live presynaptic boutons. Contrasting with fast neurotransmitters, dopaminergic (DAergic) neurons form multiple types of axonal release sites (6, 7) called varicosities, many of which are nonsynaptic and even release DA from somata and dendrites (8). DA typically diffuses considerable distances from release sites, and signal transduction by metabotropic DA receptors is much slower than signaling by fast-acting neurotransmitters via ionotropic receptors.

The distinct mode of DAergic signaling is of key functional significance and hence likely underpinned by cellular and molecular specializations of its release machinery that differ from fast-acting systems, e.g., with regard to the organization, priming, fusion, and dynamics of synaptic vesicles (SVs). Indeed, the few known examples of proteins involved in the control of DA release indicate that DAergic varicosities not only differ from typical fast-acting synapses but are also very heterogeneous in structure, function, and molecular composition (6, 9–12). To assess the function of this heterogeneous system, DA release must be examined with a spatial resolution that discriminates individual varicosities. Common electrochemical DA detection methods cannot resolve large numbers of varicosities in parallel due to their low spatial resolution, determined by electrode number, type, and position (13–15). Furthermore, genetically encoded DA sensors (16–19) have not yet been used to examine DA release from discrete varicosities with subcellular precision, though recent data indicate DA detection at discrete dendritic release sites in substantia nigra (20). We thus developed a DA detection method based on single-walled carbon nanotubes (SWCNTs), which emit photostable (21) structure-dependent fluorescence in near infrared (NIR) (870 to 2,400 nm) ideal for biological imaging (22). Functionalized SWCNTs are highly effective nanosensors (23–29), and they have been used as high-affinity DA sensors that detect DA release from cell lines (30) or in brain slices (31). However, the potential gain in spatial resolution provided by nanosensor-based approaches, e.g., to examine the spatiotemporal complexity of DA release, has not been explored, mainly because

Author contributions: S.E., N.B., S.K., and J.A.D. designed research; S.E., B.H., and J.A.D. performed research; S.E., A.A.C., A.S., F.M., and S.K. contributed new reagents/analytic tools; S.E., A.A.C., B.H., S.K., and J.A.D. analyzed data; and S.E., A.A.C., A.S., B.H., F.M., N.B., S.K., and J.A.D. wrote the paper.

The authors declare no competing interest.

This article is a PNAS Direct Submission.

[1]To whom correspondence may be addressed. Email: sebastian.kruss@rub.de or daniel@mpinat.mpg.de.

This article contains supporting information online at http://www.pnas.org/lookup/suppl/doi:10.1073/pnas.2202842119/-/DCSupplemental.

Published May 25, 2022.

primary DAergic neurons have to be differentiated in culture over several weeks for such purposes and because cultivation and adhesion on a nanosensor layer affect sensor sensitivity and cell viability. By using a sensor paint on top of mature neuronal cultures, we circumvented these challenges and now present a SWCNT-based DA detection method—adsorbed nanosensors detecting release of dopamine (AndromeDA)—that optically discriminates DA release from large numbers of neuronal release sites simultaneously.

Results

AndromeDA Detects Distinct, Heterogeneous DA Release Events from Large Populations of Discrete Varicosities. NIR fluorescent SWCNTs were functionalized with single-stranded deoxyribonucleic acid, consistent of 10 thymine and guanine repeats ($[GT]_{10}$-ssDNA) to create nanosensors that increase in fluorescence emission with reversible DA binding (*SI Appendix*, Figs. S1 and S2). To generate a two-dimensional (2D) nanosensor layer capable of high spatiotemporal resolution, we applied a concentrated solution of SWCNT-$(GT)_{10}$-ssDNA nanosensors to poly-L-lysine (PLL)–coated coverslips, resulting in a painted nanosensor surface on the glass, i.e., AndromeDA. NIR fluorescence imaging used to characterize the responsiveness of AndromeDA to DA showed fluorescence increases of up to 40% upon reversible DA binding in a concentration-dependent manner, with an half maximal effective concentration (EC_{50}) of 299 nM (*SI Appendix*, Fig. S2).

To study DA release from varicosities, we initially tried culturing neurons directly on nanosensor-coated coverslips, similar to previous experiments with PC12 cells (30), but this approach compromised neuron viability and nanosensor sensitivity. Instead, cocultured neurons from mouse hippocampus and ventral midbrain were grown on coverslips for at least 6 wk, and nanosensors were applied immediately prior to imaging. This resulted in a uniform layer on the glass surrounding the cells (Fig. 1*A*), as nanosensors did not adhere to cells (*SI Appendix*, Fig. S3). A schematic of a single nanosensor is shown in Fig. 1*B*. Atomic force microscopy (AFM) demonstrated the shape of single nanosensors and the uniformity of the nanosensor layer on a PLL-coated surface (Fig. 1*C*). Using neurons from neonatal mice, in which most DAergic neurons express enhanced green fluorescent protein (EGFP) under the tyrosine hydroxylase (TH) promoter (TH-EGFP mice) (*SI Appendix*, Fig. S4 *A–C*), we identified DAergic axons surrounded by AndromeDA using a custom-built optical setup to simultaneously image light in the visible and NIR range (*SI Appendix*, Fig. S5). By visualizing DAergic varicosities and the location of DA in time and space, AndromeDA allows the detection and separate analysis of DA release and diffusion (Fig. 1*D*).

To validate AndromeDA in a biologically relevant setting, ventral midbrain neurons were stimulated to evoke DA release (Fig. 2). Electrical field stimulation (200 pulses, 20 Hz), which induces action potential firing (32), caused a rapid increase in the extracellular NIR fluorescence of neuronal cultures, corresponding to AndromeDA activation by evoked DA release and diffusion (Fig. 2, untreated neurons). Chemical depolarization of neurons with 90 mM KCl resulted in a relatively strong and sustained increase in extracellular NIR fluorescence (Fig. 2 *A* and *B*; fluorescence quantification shown in *SI Appendix*, Fig. S6 *A–D*). AndromeDA activation throughout the extracellular space was widespread, reflecting the diffusion of DA away from release sites and the high sensitivity of the sensors (Fig. 2 *A* and *B*). To account for possible differences in the density of nanosensor layers between experiments, 100 µM DA was added to

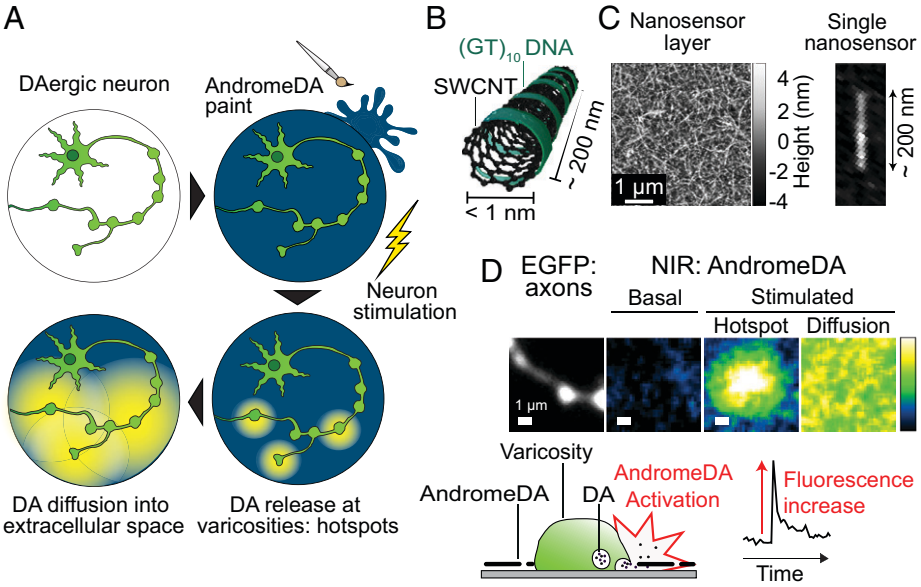

Fig. 1. AndromeDA paint as a DA sensor. (*A*) Illustration of a cultured DAergic neuron painted with AndromeDA. Neuronal stimulation results in DA release, which interacts with AndromeDA, increasing nanosensor fluorescence and thus sensing the spatiotemporal pattern of DA release and diffusion. (*B*) Schematic of the nanosensors used in AndromeDA, each consisting of a (5, 6)-SWCNT-$(GT)_{10}$ complex. (*C*) *Left:* AndromeDA consists of a dense layer of individual nanosensors, visualized here using AFM. *Right:* Magnified image of a single nanosensor, taken from a lower-density preparation of nanosensors. (*D*) *Left:* Magnified view of an EGFP-positive axon with a single varicosity in view. *Right:* AndromeDA fluorescence in the same field of view at different points in time. Initially, NIR fluorescence is low due to the lack of extracellular DA (labeled Basal). Neuronal stimulation results in the appearance of a transient AndromeDA hotspot adjacent to the varicosity (labeled Hotspot). As DA diffuses, AndromeDA is activated over a wider area, resulting in a more generalized increase in NIR fluorescence (labeled Diffusion). *Below:* Side-view schematic showing a DAergic varicosity surrounded by AndromeDA on the glass coverslip (*Left*), and fluorescence trace (*Right*) showing the NIR fluorescence change associated with the hotspot image above it.

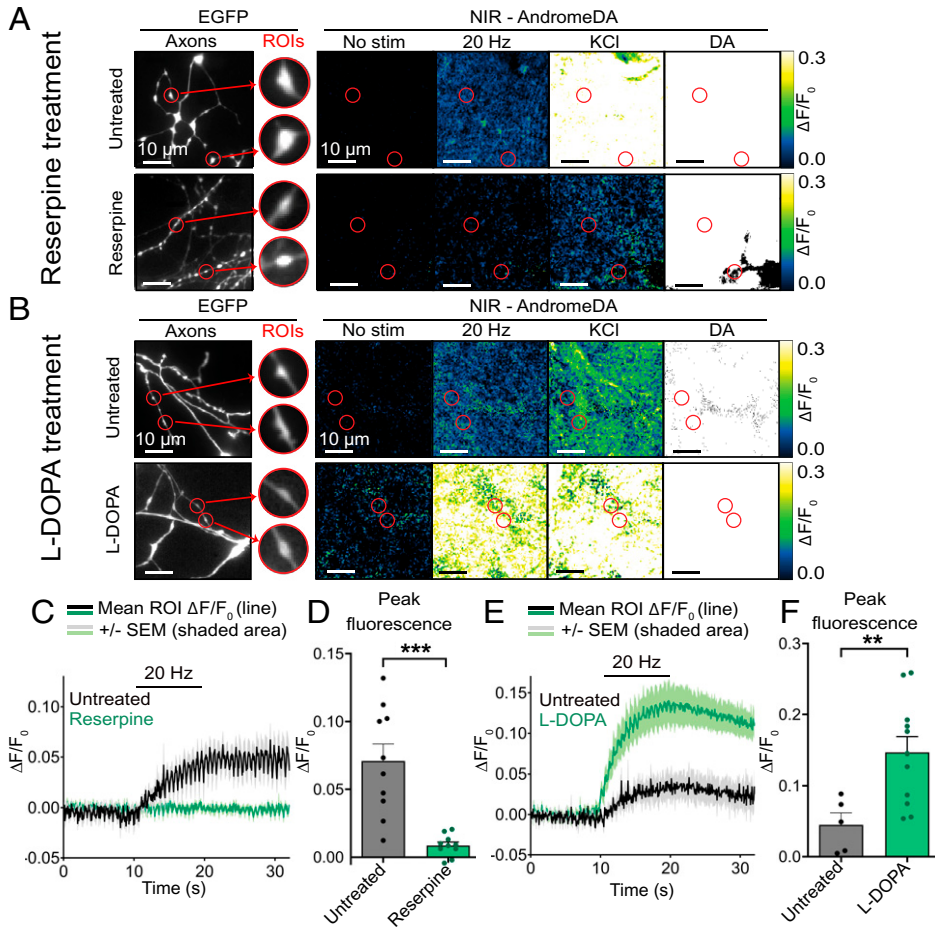

Fig. 2. Imaging of DA release and diffusion. (*A*) Images of normalized AndromeDA fluorescence (*Left* to *Right*) prior to stimulation (No stim), during 20-Hz electrical stimulation, during 90 mM KCl stimulation, and during application of 100 µM DA reveal DA release in untreated neurons (*Upper*). Treatment with reserpine (1 µM, 90 min) decreases stimulus-dependent activation of AndromeDA (*Lower*). AndromeDA fluorescence was quantified at ROIs centered on EGFP-positive varicosities (examples shown as red circles). (*B*) Neurons were either untreated or pretreated with L-DOPA (100 µM, 45 min), and experiments were performed as in *A*. (*C*) Average AndromeDA fluorescence over time for neurons stimulated at 20 Hz with and without treatment with reserpine. (*D*) Peak fluorescence (mean ± standard error of the mean [SEM]) for each stimulus method. Reserpine decreases the evoked peak AndromeDA fluorescence compared with untreated neurons. $n = 10$ untreated experiments per condition. (*E*) Average AndromeDA fluorescence over time for neurons stimulated at 20 Hz with and without L-DOPA pretreatment. (*F*) Peak fluorescence (mean ± SEM) for each stimulus method. L-DOPA increases the evoked peak AndromeDA fluorescence compared with untreated neurons. $n = 5$ (untreated) and 11 (L-DOPA) experiments (scale bars, 10 µm). In line graphs, solid lines represent mean values, and shaded areas represent SEM. Statistical comparisons used two-tailed Welch's *t* test. $^{**}P < 0.01$, $^{***}P < 0.001$. Red arrows indicate the direction of changes in the AndromeDA signal in treated neurons compared to untreated controls. Note that the intensities of DA-treated images in *A* and *B* are above the displayed fluorescence scale. *F* = Fluorescence intensity.

the samples at the end of each experiment to maximally activate the nanosensor layer (Fig. 2 *A* and *B*), and fluorescence values from electrical or chemical stimulation were then expressed as a proportion of this maximal value. Some variation between experiments in the baseline (untreated) peak responses evoked by electrical or chemical stimulation was evident (Fig. 2 *D* and *F* and *SI Appendix*, Fig. S6 *B* and *D*), which can be attributed to variation in DA release between culture batches.

Electrical stimulation did not cause any fluorescence increase in the absence of DAergic neurons (*SI Appendix*, Fig. S7 *A* and *C*), indicating that AndromeDA specifically detects secreted DA. KCl application in the absence of neurons caused a modest (~10%) increase in fluorescence (*SI Appendix*, Fig. S7 *B* and *C*), likely by altering the ionic environment, which is known to affect nanotube-based sensors (33). The KCl-mediated change when neurons were absent was significantly lower than the AndromeDA activation when DAergic neurons were present (~28%; *SI Appendix*, Fig. S7 *A* and *C*). In addition, applying AndromeDA to cultured hippocampal neurons, which do not secrete DA, and stimulating them electrically did not change AndromeDA fluorescence (*SI Appendix*, Fig. S7 *D*), even when the hippocampal neurons were preincubated in L-3,4-dihydroxyphenylalanine (L-DOPA) (*SI Appendix*, Fig. S7 *E*).

To further validate that AndromeDA specifically detects DA release, we assessed neurons treated with the vesicular monoamine transporter (VMAT) inhibitor reserpine (34), which depletes DA from SVs and abolishes DA release with prolonged incubation (35). Reserpine (1 µM, 90 min) decreased peak AndromeDA fluorescence at regions of interest (ROIs) around varicosities after electrical (~88% reduction in peak fluorescence) and KCl (~68% reduction) stimulation (Fig. 2 *A*, *C*, and *D* and *SI Appendix*, Figs. S6 *A* and *B* and S8). Complementing this, we examined the effect of L-DOPA, which increases the DA content of SVs in DAergic neurons 10-fold (36). L-DOPA (100 µM, 45 min) significantly increased peak AndromeDA activation at ROIs around varicosities when neurons were depolarized (Fig. 2 *B*, *E*, and *F* and *SI Appendix*, Figs. S6 *C* and *D* and S8). Thus, altering vesicular DA content correspondingly altered the AndromeDA signal, confirming its DA specificity.

The detection of DA diffusion in the extracellular space reflects cumulative DA release from many varicosities and does not facilitate the assessment discrete varicosities. However, in

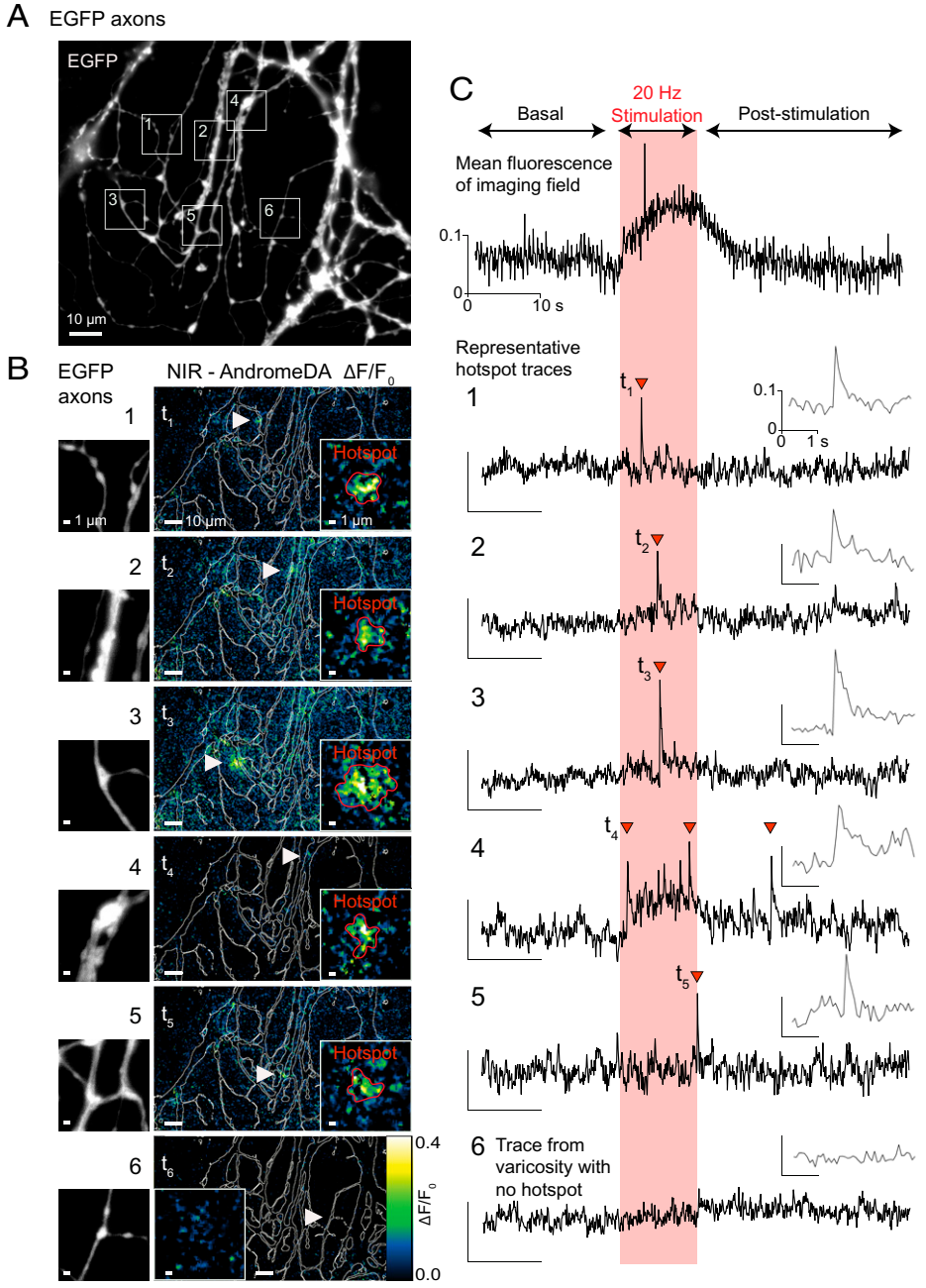

Fig. 3. Detection and analysis of AndromeDA hotspots at populations of discrete varicosities. (*A*) Field of view showing EGFP-positive DAergic axons. Five exemplary regions showing adjacent hotspots of AndromeDA fluorescence during 20-Hz electrical field stimulation are highlighted (white boxes, regions 1 to 5). (*B*) *Left:* Magnified images of exemplary EGFP-positive axonal varicosities. *Middle:* Normalized AndromeDA NIR response ($\Delta F/F_0$) at the time point of the onset (t_1 to t_5) of the indicated hotspot (white arrowheads). The outline of the EGFP-positive axon is overlaid in white, illustrating the position of the hotspot in relation to the axon. A magnified view of the hotspot is shown in the right corner (scale bar, 1 µm). Region 6 shows a representative region without detectable DA release above the diffusive background DA. (*C*) The uppermost trace shows the mean fluorescence intensity over time within a selected region of the extracellular space that contained no varicosities or hotspots. Subsequent panels show fluorescence traces corresponding to the exemplary regions shown in *B*. For regions 1 to 5, the traces show the mean fluorescence intensity within the ROI of the representative hotspots. For region 6, which contained no hotspot, the trace shows the average fluorescence of the inset NIR in *B*. The 20-Hz electrical stimulation window is highlighted in pink. Arrowheads indicate hotspot fluorescence peaks. For the scale bars in *C*, the *y* axis represents hotspot fluorescence and the *x* axis represents time. Hotspot fluorescence traces were generated by subtracting the signal of the extracellular space ($\Delta F/F_0$) from the mean signal within the hotspot ROIs ($\Delta F/F_0$) to highlight AndromeDA activation due to local DA release above overall DA diffusion.

addition to more diffuse AndromeDA activation, we observed brief, localized hotspots of increased fluorescence, generally during neuronal stimulation, above the surrounding fluorescence and generally located adjacent to varicosities (Fig. 3 *A*–*C* and Video S1). DA is stored in SVs in varicosities at very high concentrations, and DA release from a single varicosity causes a localized high DA concentration that rapidly dissipates as secreted DA diffuses into the surrounding extracellular space (8). Thus, fluorescence hotspots corresponded to the high, local DA concentration that occurs upon DA release events. Manual identification and analysis of hotspots lacked the necessary sensitivity to reliably detect small events. We thus developed a Fiji plug-in that uses machine learning to identify hotspots from NIR videos, the Dopamine Recognition Tool (DART). Imaging EGFP and NIR fluorescence in parallel, we observed up to 100 DAergic varicosities and 50 DART-identified hotspots

within a single imaging field (12,800 μm^2; Fig. 3 *A* and *B*). Hotspots were generally brief, usually between three and five imaging frames in duration (200 to 333 ms). DART automatically defined the region within each detected hotspot as a ROI (Fig. 3*B*). To isolate the fluorescence corresponding specifically to each hotspot, the mean response of the extracellular space was subtracted from the mean fluorescence within an identified hotspot, thus correcting for AndromeDA activation by DA diffusing from other release sites. After correction, hotspot traces demonstrated a characteristically fast rising phase and a slower decaying phase (Fig. 3*C*). While most varicosities did not exhibit nearby hotspots, varicosities were observed exhibiting single or multiple nearby hotspots during 20-Hz stimulation (Fig. 3*B*). Hotspots were also induced by KCl stimulation (*SI Appendix*, Fig. S9 and Video S2).

The areas and peak intensities of hotspots were highly variable, indicating a striking heterogeneity in DA release events at the level of single varicosities (Fig. 4 *A* and *B*). To further validate that hotspots represent discrete DA release events, we performed additional spatiotemporal analyses of images. An example image showing DAergic axons and the ROIs occupied by hotspots observed while imaging these axons is shown in *SI Appendix*, Fig. S10, demonstrating hotspot clustering close to axons. As DA release occurs at varicosities upon action potential firing, we hypothesized that hotspots should occur close to varicosities and be triggered by electrical stimulation. To verify the close spatial association of hotspots to DAergic varicosities, we took advantage of our high spatial resolution and measured the distance from hotspot centers to the center of the nearest varicosity as identified in the corresponding EGFP image (Fig. 4 *C* and *D* and *SI Appendix*, Fig. S11*A*). The median hotspot-varicosity distance was 1.2 μm, with ∼86% of hotspots within a 3-μm radius of a varicosity. Remaining hotspots are likely due to DA release from EGFP-negative DAergic neurons (∼30% of all TH-positive neurons; *SI Appendix*, Fig. S4). We also measured hotspot-varicosity distance using NIR and EGFP images from noncorresponding experiments, providing a randomized negative control (Fig. 4*E* and *SI Appendix*, Fig. S11*B*). In this case, hotspot-varicosity distances were significantly larger than corresponding NIR and EGFP images, verifying that hotspots generally occur close to varicosities (Fig. 4*E* and *SI Appendix*, Fig. S11*B*).

To verify the dependency of hotspots on neuronal depolarization, we first examined whether they corresponded in time with neuronal stimulation. Most hotspots (∼82%) occurred during electrical stimulation, ∼4% occurred prior to stimulation, and ∼14% occurred after stimulation had ceased (Fig. 4*F*). Thus, a large majority of hotspots occurred during exogenous neuronal stimulation (Fig. 4*G*), which we referred to as evoked hotspots. Evoked and nonevoked hotspots were quantitatively similar (Fig. 4*H*). In samples stimulated with KCl, hotspots corresponded in time with the application of KCl (*SI Appendix*, Fig. S11*C*). We next considered the cause of nonevoked hotspots. They were not the result of glutamatergic signaling in the culture, which could activate DAergic neurons, as experiments were performed in the presence of glutamate receptor antagonists. We tested the effect of 300 nM tetrodotoxin (TTX), which blocks action potentials, in the absence of electrical stimulation. Hotspots were not detected in the presence of TTX, but nonevoked hotspots appeared upon TTX removal (Fig. 4*I* and *SI Appendix*, Fig. S12 *A*–*C*). After TTX removal, neurons exhibited normal evoked DA release (*SI Appendix*, Fig. S13). These data indicate that nonevoked hotspots are caused by the spontaneous electrical activity of DAergic neurons, so that all hotspots are evoked by neuronal firing and subsequent electrically evoked DA release events. To quantify when each hotspot occurred in time, we used the time at which the hotspot peak intensity was reached. A cumulative frequency histogram plotting of the timing of hotspot occurrence in L-DOPA–treated neurons showed that most hotspots appeared within the first 4 s (80 pulses) of electrical stimulation (*SI Appendix*, Fig. S14), with hotspots becoming less frequent as 20-Hz stimulation continued. This decrease in detectable discrete DA release events with repeated stimulation may indicate a depletion of DA at varicosities. These data therefore demonstrate the utility of AndromeDA in studying in DA release dynamics across populations of individual varicosities.

Together, these data demonstrate that AndromeDA can detect and discriminate i) summed DA release in the extracellular space, representing diffusing DA from many local release sites (Fig. 2 and Video S2), and ii) discrete DA release events at single varicosities (Figs. 3 and 4). Importantly, AndromeDA detects many release events from large numbers of varicosities with subcellular resolution, a significant methodological advance for studying DA release from large numbers of sites in parallel.

To assess whether DA dynamics in our system are affected by the dopamine transporter (DAT), we simulated the contributions of DA diffusion and uptake to extracellular DA levels (*SI Appendix*, *DA Diffusion Simulation* and Figs. S15 and S16) (37). The simulation shows that the open 2.5-dimensional geometry and the fast on rate of DA binding by nanosensors (30, 38, 39) render the impact of DAT activity on our data in this experimental setting negligible.

AndromeDA Differentiates Active and Silent Varicosities. DAergic varicosities are filled with SVs (40). Interestingly, previous studies have indicated that DA release occurs only in a subpopulation of varicosities (6, 9), although DA release was measured indirectly with fluorescence-based exocytosis assays. To investigate this using a direct method of DA detection, we examined the proportion of total varicosities that exhibited spatially associated AndromeDA hotspots, which indicate local DA release events. In our analyses, the median hotspot area was 5.5 μm^2, and assuming that hotspots are approximately circular, this gives a diameter of 2.6 μm. We thus set a threshold distance of ≤3 μm for defining that a given hotspot was spatially associated with a varicosity and examined the proportion of varicosities that show discrete DA release events. In untreated neurons, hotspots were relatively infrequent, observed in only 25% of all experiments and adjacent to 13% of all varicosities on average (Fig. 4*J*). L-DOPA treatment increased hotspot frequency, with hotspots observed in all experiments and adjacent to 17% of all varicosities. L-DOPA increases the quantal size of DA release (35, 36), and thus the increase in hotspot frequency following L-DOPA treatment is likely due to increased quantal size, allowing discrete release events to register above background. While L-DOPA treatment increased hotspot frequency (Fig. 4*J*), it did not alter hotspot peak intensity or area (*SI Appendix*, Fig. S9 *A* and *B*). Similar to electrical stimulation data, only a subpopulation of varicosities showed hotspots upon KCl-mediated depolarization (*SI Appendix*, Fig. S17). These data support the notion that DA is released from only a subset of active varicosities by demonstrating the phenomenon via direct DA detection.

Local AndromeDA Responses Diminish with Distance from DAergic Axons. As axons are the source of secreted DA, AndromeDA signals are expected to be stronger closer to axons. Exploiting

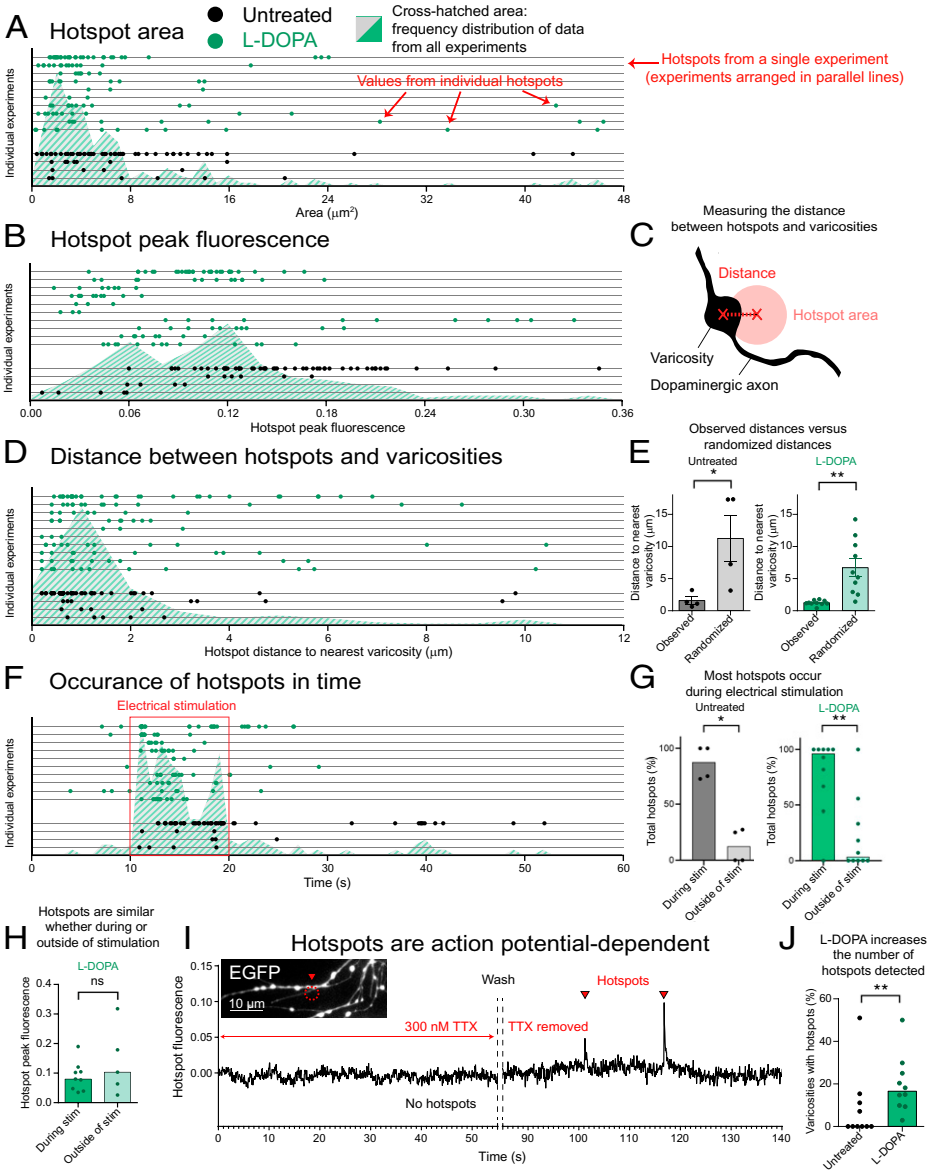

Fig. 4. Hotspots are heterogeneous sites of activity-dependent DA secretion. Hotspots observed in untreated (black dots) and L-DOPA–treated (100 μM, 45 min, green dots) electrically stimulated neurons are shown. (*A*) Area of activated AndromeDA within single hotspots. (*B*) Peak fluorescence within single hotspots. (*C*) Scheme illustrating how distance and hotspot area are defined. (*D*) Distances between the center of individual hotspots and the nearest varicosity. (*E*) Varicosity-hotspot distance was larger when noncorresponding EGFP images were used (randomized). (*F*) Time points at which individual hotspots occur. Electrical stimulation from 10 to 20 s is highlighted (red). (*G*) Hotspots occur primarily during electrical stimulation. (*H*) Hotspot peak fluorescence is no different from that of hotspots observed in the absence of stimulation. Only hotspots from neurons treated with L-DOPA were analyzed due to the large number of hotspots available for analysis compared with untreated neurons. (*I*) Hotspots are the result of spontaneous neuronal firing. The representative trace shows AndromeDA fluorescence over time from an EGFP-positive varicosity within the ROI indicated (white arrowhead). During TTX application, no hotspots are evident, but washout of TTX results in the appearance of hotspots (black arrowheads). (*J*) Only a subpopulation of varicosities exhibits closely adjacent (<3 μm) hotspots. L-DOPA treatment causes a significant increase in the proportion of varicosities with adjacent hotspots. In *E*, dots represent the median of each experiment, and column height is the mean of all experiments (± SEM). In *G*, *H*, and *J*, dots represent the median of each experiment, and column height is the median of all experiments. In *A*, *B*, *D*, and *F*, hotspots are organized on the *y* axis into individual experiments (lines), and the hatched area shows the frequency distribution of all hotspots. In *A*–*H*, data represent 68 hotspots from $n = 4$ experiments (untreated) and 110 hotspots from $n = 10$ experiments (L-DOPA). Data were compared using either two-tailed Welch's *t* test (*E*) or the Mann-Whitney test (*G*, *H*, and *J*). $^*P < 0.05$, $^{**}P < 0.01$. Hotspot traces were generated by subtracting the mean signal of the extracellular space ($\Delta F/F_0$) from the mean signal within the hotspot ROI ($\Delta F/F_0$) for each time point (scale bar, 10 μm).

the spatial resolution of AndromeDA, we quantified the local change in fluorescence during neuronal stimulation at different distances from axons (Fig. 5*A*). To do this, the background fluorescence due to DA diffusion in a region distant from the axons was subtracted from the fluorescence within each ROI around the axon, thus giving the local change in fluorescence over time. ROIs close to axons showed the greatest relative change in fluorescence, with the amplitudes of stimulus-evoked fluorescence signals decreasing with distance from the axon (Fig. 5*B*). These data highlight the rapid rise in relative fluorescence adjacent to axons that occurs with electrical stimulation, followed by a decline in fluorescence that precedes the cessation of electrical stimulation. Together with our observation that hotspots decrease in frequency during 20-Hz stimulation (*SI Appendix*, Fig. S14), these data indicate that DA release occurs rapidly following the onset of stimulation and decreases with time, indicating DA depletion at varicosities. In line with this, DA depletion has been observed using amperometry recordings in striatal slices (10–12), and repeated stimulation of DAergic neurons at 20 Hz results in depletion of SVs when assayed using synaptopHluorin (41).

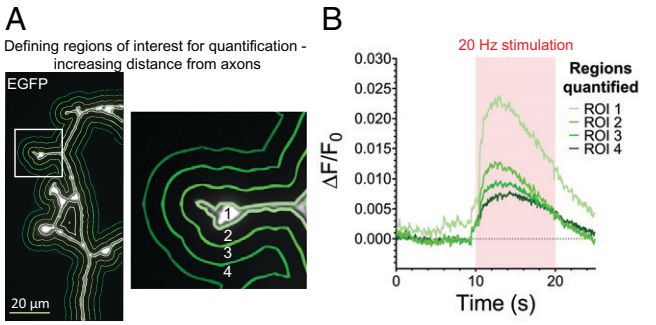

Fig. 5. AndromeDA activation decreases with distance from axons. (*A*) To examine how the local changes in AndromeDA fluorescence were influenced by distance from axons, AndromeDA fluorescence was quantified at different distances from axons. The first ROI was defined by thresholding the EGFP signal (white) of the DAergic axon and tracing it (ROI 1). The line defining the boundary of this ROI was then moved outwards by 2 µm from the axon to create ROI 2. This process was repeated to create concentric ROIs, as indicated in green and identified using numbers. (*B*) The change in the local normalized fluorescence within each ROI compared with a distant region containing no axons was quantified (*Materials and Methods*). This gave the local increase in AndromeDA fluorescence within each ROI. ROI 1, which is closest to the axon, shows a rapid, high-amplitude increase in fluorescence with electrical stimulation. As the local changes in AndromeDA fluorescence are analyzed farther from the axon, the amplitude of the response is decreased. This demonstrates that local AndromeDA activation is greatest immediately adjacent to axons and that the local DA level rises rapidly with stimulation. Traces in *B* represent average normalized fluorescence over time. ROI fluorescence values, which are colored according to the ROI they represent, were generated by subtracting the mean normalized ($\Delta F/F_0$) signal of a selection of the extracellular space from the mean signal within the ROI ($\Delta F/F_0$) for each time point. Data represent $n = 7$ independent coverslips.

Validation of AndromeDA in SV Priming–Deficient Neurons. SV priming by Munc13 proteins, which dock SVs to the presynaptic membrane and render them fusion competent (42), is absolutely required in essentially every synapse type tested so far, with Munc13 deletion causing near-complete or complete loss of neurotransmitter release (43, 44). To determine whether this also applies to synaptic DA secretion, we used AndromeDA to assess the Munc13 dependence of DA release from cultured neurons and also performed a collaborative analysis of Munc13 function in DAergic synapses using amperometry in striatal slices (12).

We used immunolabeling to assess Munc13 expression in DAergic neurons. The dominant Munc13-1 isoform was readily detected at DAergic active zones as defined by anti-bassoon colabeling (*SI Appendix*, Fig. S18). Due to the lack of effective antibodies against Munc13-2 and Munc13-3, we analyzed previously characterized knock-in (KI) mice that express Munc13-2– enhanced yellow fluorescent protein (EYFP) or Munc13-3-EGFP fusion proteins from the endogenous genetic loci (45). EGFP or EYFP immunodetection revealed no Munc13-2-EYFP–positive puncta in TH-positive DAergic axons, whereas cultured hippocampal neurons, as Munc13-2–positive controls (46, 47), showed clear signals (*SI Appendix*, Fig. S19). Similar observations were made with DAergic Munc13-3-EGFP neurons and cultured cerebellar granule neurons as positive controls (48, 49) (*SI Appendix*, Fig. S20). These data show that Munc13-1 is the dominant Munc13 in cultured murine DAergic neurons and that Munc13-2 and Munc13-3 are absent or expressed at very low levels, consistent with findings showing predominant Munc13-3 expression in hindbrain (48, 50, 51). On the other hand, Munc13-2 mRNA has been shown to be expressed in at least some mouse DAergic neurons (52). Thus, to maximize the likelihood of detecting effects of Munc13 deletion on DA release, we studied TH-EGFP neurons lacking Munc13-1 and Munc13-2 (Munc13 double knock-out, DKO) (Fig. 6*A*). The breeding scheme we used also provided neurons lacking only Munc13-1 (heterozygous for Munc13-2 expression) and ones that were heterozygous for the Munc13-1 deletion so that we were able to examine the impact of reducing Munc13-1 expression specifically (*SI Appendix*, Fig. S21). Electrically stimulated Munc13 DKO neurons showed no signal above noise level of fluorescence imaging and no hotspots, as opposed to neurons from littermate control mice (Fig. 6 *A–C* and *SI Appendix*, Fig. S21 *A* and *B*). Of the genotypes analyzed, only Munc13 DKO resulted in a significant reduction in AndromeDA activation evoked by 20-Hz stimulation (*SI Appendix*, Fig. S21 *C–E*). These data show that Munc13 proteins are required for evoked DA release and demonstrate the utility of AndromeDA in studying the molecular and cellular underpinnings of DA secretion.

Discussion

Optical DA sensing technology has recently made major progress, with the development of SWCNT-based DA nanosensors (23, 24, 30, 38) rapidly followed by genetically encoded fluorescent DA sensors (17, 18, 53, 54). Compared with electrochemistry, these methods provide many advantages, particularly

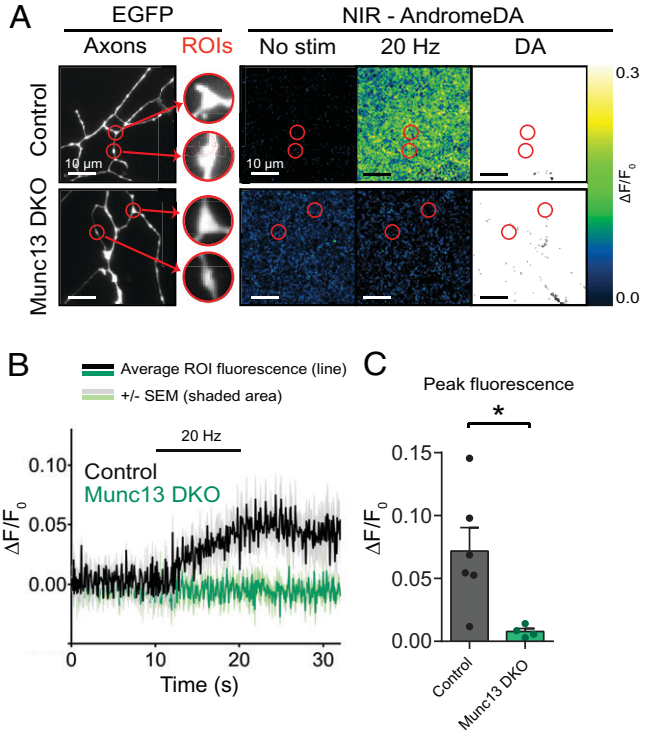

Fig. 6. Munc13-1 and Munc13-2 are required for evoked DA release. (*A*) Representative images of AndromeDA-painted ventral midbrain TH-EGFP neurons lacking expression of Munc13-1 and Munc13-2 (Munc13 DKO) compared with neurons from littermate control mice. Images show normalized AndromeDA fluorescence prior to stimulation, during 20-Hz electrical field stimulation, and during application of 100 µM DA. ROIs were defined around varicosities of EGFP-positive axons (red circles). (*B*) AndromeDA signal within ROIs over time for control and Munc13 DKO neurons with electrical stimulation. Munc13 DKO neurons exhibit no AndromeDA activation in response to electrical stimulation (red arrow indicates the loss of the AndromeDA signal in Munc13 DKO neurons). (*C*) Average maximal fluorescence peak during 20-Hz electrical field stimulation in control and Munc13 DKO neurons. For control neurons, $n = 6$, and for Munc13 DKO neurons, $n = 4$, where n represents independent experiments. In *B*, solid lines represent the mean and shaded areas represent SEM. In *C*, mean ± SEM is shown. Data were compared using two-tailed Welch's t test. *$P < 0.05$. Note that the intensities of DA-treated images in *A* are above the displayed fluorescence scale.

higher spatial resolution and multiplexing (54). While immobilized nanosensors had previously been used to detect DA release from PC12 cells (30), AndromeDA is compatible with neurons, which are of far greater biological relevance. Moreover, our combination of an immobilized sensor layer added to a mature neuron culture of EGFP-positive DAergic neurons allows the detection of DA with high spatial resolution and the correlation of DA release with subcellular structures. Nanosensors have been used previously with brain slices, but no attempt was made to ascribe DA release to particular subcellular structures (31). However, studying discrete axonal varicosities is essential to understand their functional properties and control by presynaptic proteins, whose levels vary across varicosity populations (6, 10–12). Compared with brain tissue, the low density of varicosities in neuronal culture makes the routine analysis of single varicosities and their function feasible. Such analysis of discrete DA release events in neuronal cultures has been possible with amperometry but has been restricted to a single varicosity at a time (35). Instead, AndromeDA permits the analysis of large populations of varicosities in parallel. The DA affinity of AndromeDA is similar to that of DA receptors (55), thus providing a spatiotemporal readout of DA in the biologically relevant concentration range. Additionally, the ability to tune the properties of SWCNT-based DA nanosensors expands their potential utility in addressing different aspects of DA release (38). AndromeDA can be applied to mature neuronal cultures with no detectable impact on cell viability. As such, AndromeDA is readily applicable to in vitro cellular models of human disease in which varicosity function and DA release are suspected to be abnormal, such as neurons derived from Parkinson's disease patients. Our development of a machine learning–based tool, DART, for the detection of DA release events also greatly enhances the ability of our method to identify discrete sites of release.

Multiple tools have been developed to study DA exocytosis at the level of single varicosities, including styryl dyes (6), a false fluorescent neurotransmitter (9), and pHluorin-based probes (56). While these have provided important insights into DA biology, they do not report DA release itself or the movement of DA after release. Still, such exocytosis assays in neuronal culture (6) and striatal slices (9) indicated high functional heterogeneity of DAergic varicosities, with many appearing to be functionally silent and the remaining active ones exhibiting different functional properties. Using AndromeDA, we now provide direct proof that most DAergic varicosities do not release DA. We found that after treating neurons with L-DOPA to boost hotspot detection, only ∼17% of all varicosities exhibited hotspots. Validating our method, this is strikingly similar to the proportion of DAergic varicosities that exhibit electrically evoked release of the false fluorescent neurotransmitter FFN200 in the striatum (∼17%) (9). In essence, our data based on the direct detection of DA confirm that silent varicosities are an inherent property of DAergic neurons. We observed no morphological differences between varicosities that exhibit nearby adjacent hotspots and those that lack them. Given the sparse distribution of molecular components necessary for DA release (6, 10–12), we presume that differential DA release between varicosities is determined by differential configuration of the molecular SV fusion machinery in these varicosities. Moreover, individual AndromeDA hotspots were entirely driven by action potentials and varied considerably in their timing, amplitude, and area, directly demonstrating the heterogeneity of DA release. Our data further show that spontaneous action potential firing in DAergic neurons drives sufficient DA release to be visualized as discrete hotspots. Such spontaneous pacemaker firing is an inherent property of DAergic neurons (8, 57). Importantly, these data could only be provided by a method capable of examining DA release events from large numbers of varicosities in parallel, highlighting the utility of AndromeDA for interrogating fundamental aspects of DA release. The biological role of the functional heterogeneity of DAergic varicosities is unknown, but it is likely that the spatial and temporal patterns of DA release arising due to DA release from a functionally diverse varicosity population are important in DA signaling and information processing.

Stimulation of DAergic neurons resulted in a steep rise in extracellular AndromeDA fluorescence, consistent with rapid evoked DA release, and hotspots were observed primarily within the first few seconds of repeated stimulation. However, the rise in extracellular fluorescence around axons (Figs. 2 and 5) occurs faster than the emergence of hotspots in time, which do not begin to appear until after 1 s of stimulation (*SI Appendix*, Fig. S14). This indicates that hotspots do not represent every DA release event. Hotspots cross the threshold of detection presumably due to more DA being released, as highlighted by the increase in hotspots seen when neurons are treated with L-DOPA. DART is highly stringent in hotspot detection, so that some bona fide DA release events may not be detected as a result. The reason why certain release events are large enough to be detected as hotspots is unclear. These events may correspond to several release events occurring within a short time frame or to so-called complex DA release events, which result in more DA release from SVs (58). It is unlikely that hotspots correspond to DA release from large dense-core vesicles, given that DA release occurs almost entirely from SVs (35, 58, 59). Moreover, the AndromeDA DA optical detection method reports discrete DA release events with subcellular resolution, allowing a characterization of the functional properties of individual DAergic varicosities.

The speed and fidelity of signaling by fast-acting neurotransmitters is ensured by a specialized molecular machinery that regulates synaptic exocytosis, endocytosis, and SV dynamics. Given the unique features of DAergic neurotransmission, it has been assumed that specific molecular determinants define the DA release machinery. Indeed, recent studies showed that synaptotagmin-1 and Rab3-interacting molecules (RIMs) are required for DA release (10, 11), as is the case for the fast-acting neurotransmitter glutamate, while the active zone protein ELKS is not required (10). We found that the genetic deletion of Munc13-family SV priming proteins abolishes evoked DA release. In accord with the well-defined, essential role of Munc13s in vesicle priming in multiple other neuronal and endocrine systems, this documents an essential SV priming function of Munc13s in DAergic synapses. Similar observations were made in a parallel study in striatal slices, leading to the conclusion that DAergic synapses require SV priming and release-site scaffolding by Munc13s, RIMs, and Liprins, whereas multiple other presynaptic components are dispensable (12). Most importantly, in the context of the method-development focus of our study, our present analysis of Munc13-deficient neurons documents the major utility of AndromeDA as a tool to study the molecular and cellular underpinnings of DA secretion. In the future, it will facilitate detailed analysis of how molecules shape the heterogeneity of DA release across populations of individual varicosities.

By allowing high-resolution imaging of DA release from many release sites, AndromeDA paves the way for a deeper understanding of DAergic signaling at a subcellular level.

AndromeDA represents a tool that will provide fundamental insights into the basic properties of DA secretion, into the heterogeneity and plasticity of DA release, and into the detailed molecular processes that shape DA release. In principle, our painting approach to generating 2D sensor layers such as AndromeDA can also be applied to other neurotransmitter nanosensors, such as our recently developed serotonin sensor (25). Such high-resolution approaches are essential to decipher the complex physiological and pathophysiological functions of DA and other modulatory neurotransmitters.

Materials and Methods

Animals. Mouse lines, genotyping, housing, and ethics are provided in *SI Appendix, Extended Materials and Methods*.

Preparation of Primary Neuron Cocultures. To prepare neurons intended for AndromeDA imaging, a coculture protocol was established by combining dissociated hippocampal primary neurons with ventral midbrain neurons in a single-cell culture system. Hippocampal neurons, cultured 5 to 7 days prior to the addition of ventral midbrain neurons, promoted DAergic neuron survival for at least 6 wk. This period of survival is comparable to the classical ventral midbrain neuronal preparation grown on glial cells (60–62), and it provided the areas of cell-free glass necessary for AndromeDA application.

For neuron culture, glass coverslips (25 mm, #1 Menzel Gläser) were coated in 0.0008% (wt/vol) PLL (Sigma-Aldrich, P4707) in phosphate-buffered saline (PBS). Hippocampal neurons were then prepared as previously described (63), seeded at 1.5×10^5 neurons per coverslip in neuron medium (2% fetal bovine serum [FBS], 2% B-27 [Gibco, 17504-044], penicillin [200 U/mL]/streptomycin [200 μg/mL] [Gibco, 15140-130], 2 mM GlutaMAX [Gibco, 35050-038] in Neurobasal-A), and incubated at 37 °C with 5% CO_2. The next day, the medium was replaced with neuron medium supplemented with 67 μg/mL 5-fluorodeoxyuridine (Sigma-Aldrich) and 165 μg/mL uridine (Sigma-Aldrich) to inhibit cell proliferation.

After 7 d, ventral midbrain neurons were prepared using a protocol based on two methods described previously (6, 62). Ventral midbrains of mice at postnatal day 0 (P0) were dissected and digested with papain at 34 °C for 45 min, followed by 15 min of incubation in trituration medium (10% FBS in Neurobasal-A medium [NBA]). After trituration, cell suspensions were centrifuged (5 min, 1,500 rpm). Cells were resuspended in neuron medium and seeded (1.5×10^5 cells/coverslip) on top of the hippocampal neurons. Human glial-derived neurotrophic factor (GDNF; Alomone Labs, G-240) was added to the wells (10 ng/mL). The next day, the medium was exchanged with preconditioned neuron medium containing 67 μg/mL 5-fluorodeoxyuridine, 165 μg/mL uridine, and 10 ng/mL GDNF. Neuron medium was preconditioned by incubation for 24 h on primary cultures of cortical glial cells (63). Ventral midbrain neurons were allowed to mature for 3 to 6 wk before their use in AndromeDA experiments. Ventral midbrain neuron cultures from Munc13 DKO mice and their littermate controls were prepared from mouse embryos at embryonic day 18 (E18), since Munc13 DKO neonates are not viable at birth.

For analysis of Munc13 expression, ventral midbrain neurons were seeded on glass coverslips containing a monolayer of glial cells (60–62). For analysis of Munc13-1, midbrain neurons from C57BL/6 P0 mice were used, and neurons from Munc13 DKO mice served as negative control for Munc13-1 immunolabeling. For analysis of Munc13-2 and Munc13-3, ventral midbrain neurons from P0 Munc13-2-EYFP KI and P0 Munc13-3-EGFP mice, respectively, were used. As a positive control for immunolabeling against Munc13-2-EYFP, hippocampal neurons were prepared from Munc13-2-EYFP KI mice and seeded on glial monolayers. As a positive control for immunolabeling against Munc13-3-EGFP, cerebellar granule neurons were prepared from P0 Munc13-3-EGFP KI mice and seeded on PLL-coated glass coverslips without glia, based on a published method (64).

Synthesis of $(GT)_{10}$–Functionalized SWCNTs. Chirality-enriched (5, 6)-SWCNTs (Sigma-Aldrich, 704148) were suspended in water (9 mg/mL). Approximately three flakes of SWCNTs were then added to 500 μL of D_2O-PBS, prepared with heavy water (Sigma-Aldrich, 368407) and containing 200 pmol/μL $(GT)_{10}$ oligonucleotides. Heavy water improves the separation of solubilized single DNA-SWCNT complexes during centrifugation. Oligonucleotides were synthesized by the DNA Core Facility of the Max Planck Institute for Multidisciplinary Sciences, Göttingen, Germany, using a medium-throughput oligo synthesizer (Dr. Oligo 48, Biolytic Lab Performance Inc.) and purified by reverse-phase, high-pressure liquid chromatography (PerSeptive Biosystems).

A stable dispersion of SWCNTs was achieved based on previously published protocols (30, 38) through tip sonication for 1 h at 30% power at 4 °C (Fisher Scientific Model 120 Sonic Dismembrator, Fisherbrand Probe 12921181, tip size 2 mm). SWCNT-$(GT)_{10}$ complexes were separated from nonfunctionalized SWCNTs by centrifugation (16,000 rpm for 30 min at 4 °C). The supernatant containing SWCNT-$(GT)_{10}$ complexes was collected; this centrifugation enrichment step was repeated twice, and the final supernatant was used as a nanosensor stock.

UV-Vis-NIR Absorption and NIR Fluorescence Spectroscopy. The nanosensor stock concentration was determined by measuring the absorption spectrum in PBS (*SI Appendix*, Fig. S22) with an ultraviolet-visible (UV-vis)-NIR spectrometer (JASCO V-670, Spectra Manager Software) and integrating the area below the (5, 6) peak using the molar extinction coefficient at 991 nm and an estimated length of 200 nm (65). The concentration was adjusted to 300 nM, and the stock was stored at 4 °C for up to 3 wk. NIR fluorescence spectra (*SI Appendix*, Fig. S1) of nanosensors were acquired with a Shamrock 193i spectrometer (Andor Technology) on an IX53 microscope (Olympus). Then, 200 μL of nanosensor suspension in a 96-well plate was excited through a monochromator, at 560 nm, connected to a LSE341 light source (LOT-Quantum Design). NIR fluorescence spectra were taken before and after the addition of 100 μM DA.

Microscope Configuration. A custom-built system based on an Olympus IX53 microscope was used for NIR imaging, using a 100x oil-immersion objective (UPLSAPO100XS, Olympus). The system used two cameras for simultaneous imaging of NIR and visible light. Visible light fluorescence was excited using an xCite 120Q (Excelitas Technologies) and imaged using an Andor Zyla 5.5 camera (Andor Technology). NIR fluorescence was excited using a 561-nm laser (Cobolt Jive, Cobolt AB; Pmax. = 500 mW) and imaged using a Xenics Cheetah-640-TE1 InGaAs camera (Xenics). NIR imaging (>900 nm) was performed at 15 frames/s for all live-cell experiments. A schematic describing the optical components and configuration of the system is provided (*SI Appendix*, Fig. S5).

Application of AndromeDA and Live-Cell Image Acquisition. For imaging, a coverslip containing cultured neurons was washed with imaging buffer (136 mM NaCl, 2.5 mM KCl, 2 mM $CaCl_2$, 1.3 mM $MgCl_2$, 10 mM HEPES, and 10 mM D-glucose, pH 7.4). Imaging buffer was removed and 10 μL of SWCNT-$(GT)_{10}$ nanosensor stock was applied to the coverslip. Nanosensors immediately adsorb to the coverslip glass around the neurons, so the coverslip was washed immediately to remove unbound nanosensors. We refer to the 2D layer of nanosensor paint created through this process as AndromeDA.

The coverslip was mounted in an open-bath imaging chamber with integrated parallel-field stimulation electrodes (RC21-BRFS, Warner Instruments), facilitating the rapid addition of KCl and DA to the chamber during imaging. Experiments were performed at 21 °C. Imaging buffer was supplemented with 10 μM 2,3-dihydroxy-6-nitro-7-sulfamoyl-benzo(f)quinoxaline (an α-amino-3-hydroxy-5-methyl-4-isoxazolepropionic acid [AMPA]/kainate receptor antagonist), 50 μM (2R)-amino-5-phosphonopentanoate (an N-methyl-D-aspartate [NMDA] receptor antagonist), and 10 μM sulpiride (a dopamine D2 receptor antagonist), ensuring that the DA release was not a product of circuit activity from glutamatergic neurons in the culture. Sulpiride was included to prevent autoinhibition of DA release.

Neurons were electrically stimulated by field stimulation, delivering 200 square-wave biphasic pulses at 20 Hz (2-ms duration, 16 V) from a Stimulus Generator 4000 (Multichannel Systems) through parallel electrodes. For chemical depolarization, 3 M KCl was added to the chamber and rapidly mixed by pipetting (final K^+ concentration = 90 mM).

Experiments typically followed this format: imaging with field stimulation, wash, imaging with KCl stimulation, wash, and then imaging with 100 μM DA addition. For 100 μM DA treatment, 1 mM DA (freshly dissolved) was added to the chamber to a final chamber concentration of 100 μM after mixing. 100 μM DA provided a measurement of the maximal AndromeDA response (*SI*

Appendix, Fig. S3), and normalization against this value allowed for correction for variations in maximum fluorescence among individual nanosensor batches. Protocols were performed only once for each coverslip. If not stated otherwise, neurons were compared with littermates only.

For imaging experiments with reserpine (Tocris Bioscience), reserpine was added to the medium (1 μM) of midbrain neurons and incubated for 90 min before experimentation (37 °C, 5% CO_2) (66). AndromeDA was then applied and imaging experiments were conducted in the presence of fresh 1 μM reserpine. For L-DOPA (Tocris Bioscience) treatment, L-DOPA was added to the culture medium (100 μM) and the cells were incubated for 45 min (37 °C, 5% CO_2) (35, 58), after which the cells were switched to fresh imaging buffer before AndromeDA application. Imaging was conducted in the absence of L-DOPA because the nanosensors respond to L-DOPA (23). In some experiments, action potential firing was inhibited using 300 nM TTX. 300 nM TTX is routinely used in our laboratory to inhibit action potential firing in neurons, and it washes out within 5 s. Imaging was carried out for 5 min in the presence of TTX in imaging buffer, followed by washing of the coverslip, replacement of the buffer with fresh imaging buffer, and imaging of stimulated DA release as described above.

To minimize data variability across experiments, we recommend checking the nanosensor stock concentration based on the UV-vis-NIR absorption spectra to ensure that a consistent 300 nM concentration is applied to coverslips. Nanosensors should be stored at 4 °C and kept for no longer than a week before preparing a fresh stock or centrifuging to remove aggregates. Nanosensors should be applied to the coverslip briefly, and for a consistent time (~3 s), before thorough washing to remove unbound nanosensors. We further recommend counting the midbrain neurons prior to plating and mixing well before the neurons settle on the coverslip to help generate a relatively consistent neuronal density on the coverslips to minimize biological variability in experiments.

DA Dose-Response Experiments. The dose dependency of the AndromeDA response to DA was determined by applying increasing concentrations of DA (0.1 nM, 1 nM, 10 nM, 100 nM, 1 μM, 10 μM, and 100 μM) to AndromeDA-coated glass coverslips. Coverslips were mounted in a closed imaging chamber and perfused with PBS (0.5 mL/min). DA solutions were prepared fresh and only used for up to 15 min to minimize oxidation. While imaging, a coverslip was perfused with each DA concentration in ascending order, with 10 min of washing by perfusion in between each DA concentration. The imaging region was not changed during each experiment. NIR images were acquired at 1 frame/s and normalized as described below, and pixel mean intensity values were collected from the entire image using the measure stack function in Fiji. The AndromeDA EC_{50} dose-response curve (*SI Appendix*, Fig. S3) was calculated by plotting the peak NIR fluorescence response to each DA concentration and fitting a sigmoidal curve using nonlinear regression in GraphPad Prism.

Image Processing: Normalization. NIR images were analyzed using Fiji (2.0.0-rc69/1.52u/Java 1.8.0_172, 64 bit) with custom-written plugins (available from the authors). NIR image sequences were converted to 16-bit image stacks. A background image, acquired by capturing a frame of the buffer-filled imaging chamber without cells, was subtracted from all images to adjust for variations in ambient light on different days of imaging. The initial fluorescence of each pixel, F_0, was calculated for each NIR image sequence as the intensity of the projected mean image of the first 10 frames. For each pixel, the fluorescence intensity was normalized as follows. For a given image in the image sequence F_n, the normalized fluorescence change for every pixel is calculated:

$$F_n = (F - F_0)/F_0,$$

where F is the intensity value of the pixel for the image being considered and F_0 is the initial fluorescence. Normalized image sequences were then used for analysis.

Image Processing: Selection of Areas for AndromeDA Imaging. Areas of the coverslip containing no AndromeDA due to coverage by neurons (*SI Appendix*, Fig. S2) were excluded from analysis. The camera used to image EGFP (complementary metal oxide semiconductor, CMOS) has a larger sensor than the camera used to image NIR fluorescence (InGaAs). EGFP images were thus cropped and scaled to overlay with the NIR field of view, ensuring that EGFP and NIR images corresponded in space.

A single microscopic field of view was imaged in an experiment. To account for variations in axonal density, we analyzed NIR fluorescence only within 2 μm (10 pixels) around morphologically defined varicosities. Average fluorescence intensity within the ROIs was measured in each normalized image series calculated and plotted over time. A curve was then fit to the first 10 s of the resulting time trace, which represented the AndromeDA fluorescence baseline. This baseline curve was subtracted from the entire plot of fluorescence vs. time to account for any decline in AndromeDA fluorescence intensity over time.

DART: A Machine Learning–Based Tool to Detect Hotspots of AndromeDA Activation. Hotspots were defined as localized, transient increases in AndromeDA fluorescence above the surrounding fluorescence signal. We developed a semiautomated, unbiased approach to their detection. DART is a Java object-oriented language algorithm, which runs as a plugin in Fiji and uses a hybrid approach combining computer vision and machine learning in hotspot detection (67). DART attempts to correct for fluorescence loss and flickering for enhanced detection of events. DART then uses a background subtraction approach for foreground detection of bright events in the image sequence (68, 69).

To discriminate bright pixels arising due to noise from pixels associated with true hotspots, DART attempts to reduce image noise via a machine learning–based calculation of the threshold for the subtracted image for the subtraction processes described above. Noise reduction is carried out through a series of machine-based decision-making steps that involves thresholding, median filtering, and eroding. As a result, a binary image is formed consisting of true events as larger white pixel areas and false events as smaller white pixel areas (resulting from noise) over a black background. To separate between true and false events, an erosion operation takes place with a kernel dimension [3 × 3], forming a binary image that is noise free. The algorithm then uses the eroded binary image to detect, segment, and label the white areas as individual events (hotspots). The segmentation process executes using an algorithm similar to the seed fill algorithm (70), called a wave-spread function (WSF). This recursive WSF scans the image horizontally from left to right and then repeats the scan until it reaches the end of the image. Detected white pixels get a specific region identity (ID) number. Upon storing a pixel, the algorithm spreads the same process to the next neighboring connected pixels. All connected pixels get the same region ID number. The spread process is organized according to a pixel compass of an 8-point connection to identify separate event locations and durations over time. The algorithm also attempts to compensate for mechanical drifts, noise, and segmentation error by applying a user-defined search radius to search through previous white regions' center coordinates and determine whether they belong to the same events or new ones. Event ID numbers are then assigned based on this process. DART is available on request from the authors.

Image Processing: Analysis of NIR Nanosensor Fluorescence at Discrete Release Hotspots. DART was used to define ROIs containing AndromeDA hotspots. DART ROIs were then applied to normalized NIR movies. DART ROIs were manually verified to ensure that the ROIs contained bona fide hotspots of localized, transient AndromeDA activation. To correct for the activation of AndromeDA in the extracellular space by DA diffusion, the mean fluorescence intensity was measured in a region containing no axons. For each frame, the hotspot fluorescence was calculated as follows:

$$\Delta F/F_0(\textit{Hotspot DART ROI}) - \Delta F/F_0(\textit{Extracellular space}).$$

The resulting fluorescence values for each DART ROI were plotted as a time sequence describing the relative increase in NIR fluorescence above AndromeDA activation due to diffusing DA. This method highlights local, transient increases in nanosensor fluorescence that would result from DA release events. For representative images of hotspots (Fig. 3 and *SI Appendix*, Fig. S12), a Gaussian filter was applied to images to improve image clarity.

Immunocytochemistry. Detailed immunocytochemistry materials and methods are provided in *SI Appendix, Extended Materials and Methods*.

AFM. AFM was conducted in intermittent-contact mode (scan rate = 0.5 Hz, 512 lines) using an Asylum Research MFP-3D Origin instrument equipped with rectangular cantilevers (Opus, MikroMasch Europe; Al coating, tetrahedral tip, ν_{res} = 300 kHz, k = 26 N·m^{-1}). Freshly cleaved muscovite mica was coated with PLL, treated briefly with nanosensors, washed, and dried using a N_2 stream before sample measurement. Sample analysis was performed using Gwyddion.

Statistical Analysis. All statistical analyses were performed using Prism 8 (GraphPad). Sample size and independence are described in the figure legends. Where appropriate, data were analyzed for normality of distribution using the Shapiro-Wilk normality test. For normally distributed data, samples were compared using unpaired two-tailed Welch's *t* test or a Brown-Forsythe and Welch ANOVA depending on sample size. For nonparametric data, the Mann-Whitney or the Kruskal-Wallis test was used depending on sample size. The significance level was set at $P < 0.05$. An experimental sample (i.e., a given coverslip) was excluded from analysis if no induced increase in nanosensor fluorescence was observed during KCl stimulation or the final addition of 100 μM DA to each coverslip at the end of the experiment. NIR image sequences that were obscured through *x-y* drift or other obstacles such as air bubbles in the imaging chamber were excluded from analysis.

Data Availability. The Java archive file for the DART plugin for Fiji (DOI: 10.5281/zenodo.6406536) (67), as well as the code for the DA diffusion simulation and the data for the corresponding figures (DOI: 10.5281/zenodo.6406318) (37), can be accessed on Zenodo. Raw data (images) are available from the corresponding authors upon reasonable request. All other study data are included in the article and/or supporting information.

ACKNOWLEDGMENTS. We thank H. Taschenberger, N. Lipstein, P. Robinson, S. Rizzoli, J. Heathers, A. Sigler, F. Benseler, M. Cousin, P. Kaeser, and members of the Janshoff laboratory for their essential insights regarding neuron culture, data analysis, and experimental procedures. We thank C. Imig, N. Lipstein, F. Benseler, and the DNA Core Facility of the Max Planck Institute for Multidisciplinary Sciences for their assistance with the maintenance of the various mouse lines used here. We thank P. Lingor, K. Kobayashi, and Riken for providing us with the TH-EGFP mouse line. We thank A. Spreinat and C. Geisler for help with the imaging system. This work was funded by the European Commission (ERC Advanced Grant SynPrime to N.B.) and the Deutsche Forschungsgemeinschaft (DFG) grant under Germany's Excellence Strategy (EXC 2067/1-390729940 to N.B. and EXC 2033-390677874-RESOLV to S.K.). We thank the DFG for funding (KR 4242/7-1) and support via the Heisenberg Programme (to S.K.)

Author affiliations: [a]Department of Molecular Neurobiology, Max Planck Institute for Multidisciplinary Sciences, 37075 Göttingen, Germany; [b]Göttingen Graduate School for Neurosciences, Biophysics, and Molecular Biosciences, University of Göttingen, 37077 Göttingen, Germany; [c]Synapse Biology Group, Department of Molecular Physiology and Cell Biology, Leibniz-Forschungsinstitut für Molekulare Pharmakologie, 13125 Berlin, Germany; [d]Department of Cellular Neurophysiology, Center for Integrative Physiology and Molecular Medicine, Saarland University, 66421 Homburg, Germany; [e]Institute for Neuro- and Sensory Physiology, University Medical Center, 37073 Göttingen, Germany; [f]Physical Chemistry II, Faculty of Science, Ruhr University, 44801 Bochum, Germany; [g]Institute of Physical Chemistry, University of Göttingen, 37077 Göttingen, Germany; and [h]Biomedical Nanosensors, Fraunhofer Institute of Microelectronic Circuits and Systems, 47057 Duisburg, Germany

1. J.-H. Baik, Dopamine signaling in reward-related behaviors. *Front. Neural Circuits* **7**, 152 (2013).
2. W. Schultz, Multiple dopamine functions at different time courses. *Annu. Rev. Neurosci.* **30**, 259–288 (2007).
3. A. A. Grace, Dysregulation of the dopamine system in the pathophysiology of schizophrenia and depression. *Nat. Rev. Neurosci.* **17**, 524–532 (2016).
4. R. A. Wise, M. A. Robble, Dopamine and addiction. *Annu. Rev. Psychol.* **71**, 79–106 (2020).
5. S. Przedborski, The two-century journey of Parkinson disease research. *Nat. Rev. Neurosci.* **18**, 251–259 (2017).
6. J. A. Daniel, S. Galbraith, L. Iacovitti, A. Abdipranoto, B. Vissel, Functional heterogeneity at dopamine release sites. *J. Neurosci.* **29**, 14670–14680 (2009).
7. L. Descarries, K. C. Watkins, S. Garcia, O. Bosler, G. Doucet, Dual character, asynaptic and synaptic, of the dopamine innervation in adult rat neostriatum: A quantitative autoradiographic and immunocytochemical analysis. *J. Comp. Neurol.* **375**, 167–186 (1996).
8. D. Sulzer, S. J. Cragg, M. E. Rice, Striatal dopamine neurotransmission: Regulation of release and uptake. *Basal Ganglia* **6**, 123–148 (2016).
9. D. B. Pereira *et al.*, Fluorescent false neurotransmitter reveals functionally silent dopamine vesicle clusters in the striatum. *Nat. Neurosci.* **19**, 578–586 (2016).
10. C. Liu, L. Kershberg, J. Wang, S. Schneeberger, P. S. Kaeser, Dopamine Secretion Is Mediated by Sparse Active Zone-like Release Sites. *Cell* **172**, 706–718.e15 (2018).
11. A. Banerjee, J. Lee, P. Nemcova, C. Liu, P. S. Kaeser, Synaptotagmin-1 is the Ca^{2+} sensor for fast striatal dopamine release. *eLife* **9**, e58359 (2020).
12. A. Banerjee *et al.*, Molecular and functional architecture of striatal dopamine release sites. *Neuron* **110**, 248–265.e9 (2021).
13. A. Jaquins-Gerstl, A. C. Michael, A review of the effects of FSCV and microdialysis measurements on dopamine release in the surrounding tissue. *Analyst (Lond.)* **140**, 3696–3708 (2015).
14. D. L. Robinson, A. Hermans, A. T. Seipel, R. M. Wightman, Monitoring rapid chemical communication in the brain. *Chem. Rev.* **108**, 2554–2584 (2008).
15. G. Tomagra *et al.*, Quantal release of dopamine and action potential firing detected in midbrain neurons by multifunctional diamond-based microarrays. *Front. Neurosci.* **13**, 288 (2019).
16. A. Muller, V. Joseph, P. A. Slesinger, D. Kleinfeld, Cell-based reporters reveal in vivo dynamics of dopamine and norepinephrine release in murine cortex. *Nat. Methods* **11**, 1245–1252 (2014).
17. F. Sun *et al.*, A genetically encoded fluorescent sensor enables rapid and specific detection of dopamine in flies, fish, and mice. *Cell* **174**, 481–496.e19 (2018).
18. T. Patriarchi *et al.*, Ultrafast neuronal imaging of dopamine dynamics with designed genetically encoded sensors. *Science* **360**, eaat4422 (2018).
19. D. Lee *et al.*, Temporally precise labeling and control of neuromodulatory circuits in the mammalian brain. *Nat. Methods* **14**, 495–503 (2017).
20. A. F. Condon *et al.*, The residence of synaptically released dopamine on D2 autoreceptors. *Cell Rep.* **36**, 109465 (2021).
21. S. M. Bachilo *et al.*, Structure-assigned optical spectra of single-walled carbon nanotubes. *Science* **298**, 2361–2366 (2002).
22. A. M. Smith, M. C. Mancini, S. Nie, Bioimaging: Second window for in vivo imaging. *Nat. Nanotechnol.* **4**, 710–711 (2009).
23. S. Kruss *et al.*, Neurotransmitter detection using corona phase molecular recognition on fluorescent single-walled carbon nanotube sensors. *J. Am. Chem. Soc.* **136**, 713–724 (2014).
24. M. Dinarvand, S. Elizarova, J. Daniel, S. Kruss, Imaging of monoamine neurotransmitters with fluorescent nanoscale sensors. *ChemPlusChem* **85**, 1465–1480 (2020).
25. M. Dinarvand *et al.*, Near-infrared imaging of serotonin release from cells with fluorescent nanosensors. *Nano Lett.* **19**, 6604–6611 (2019).
26. J. D. Harvey *et al.*, A carbon nanotube reporter of miRNA hybridization events in vivo. *Nat. Biomed. Eng.* **1**, 0041 (2017).
27. G. Bisker *et al.*, Protein-targeted corona phase molecular recognition. *Nat. Commun.* **7**, 10241 (2016).
28. H. Wu *et al.*, Monitoring plant health with near-infrared fluorescent H_2O_2 nanosensors. *Nano Lett.* **20**, 2432–2442 (2020).
29. T. T. S. Lew *et al.*, Species-independent analytical tools for next-generation agriculture. *Nat. Plants* **6**, 1408–1417 (2020).
30. S. Kruss *et al.*, High-resolution imaging of cellular dopamine efflux using a fluorescent nanosensor array. *Proc. Natl. Acad. Sci. U.S.A.* **114**, 1789–1794 (2017).
31. A. G. Beyene *et al.*, Imaging striatal dopamine release using a nongenetically encoded near infrared fluorescent catecholamine nanosensor. *Sci. Adv.* **5**, eaaw3108 (2019).
32. T. A. Ryan, H. Reuter, S. J. Smith, Optical detection of a quantal presynaptic membrane turnover. *Nature* **388**, 478–482 (1997).
33. D. P. Salem *et al.*, Ionic strength-mediated phase transitions of surface-adsorbed DNA on single-walled carbon nanotubes. *J. Am. Chem. Soc.* **139**, 16791–16802 (2017).
34. K. D. Kozminski, D. A. Gutman, V. Davila, D. Sulzer, A. G. Ewing, Voltammetric and pharmacological characterization of dopamine release from single exocytotic events at rat pheochromocytoma (PC12) cells. *Anal. Chem.* **70**, 3123–3130 (1998).
35. E. N. Pothos, V. Davila, D. Sulzer, Presynaptic recording of quanta from midbrain dopamine neurons and modulation of the quantal size. *J. Neurosci.* **18**, 4106–4118 (1998).
36. E. Pothos, M. Desmond, D. Sulzer, L-3,4-dihydroxyphenylalanine increases the quantal size of exocytotic dopamine release in vitro. *J. Neurochem.* **66**, 629–636 (1996).
37. B. Hill, DA Diffusion Simulation for: A fluorescent nanosensor paint reveals the heterogeneity of dopamine release from neurons at individual release sites. Zenodo. https://zenodo.org/record/6406318#.YnwBKejMLcs. Deposited 1 April 2022.
38. F. A. Mann, N. Herrmann, D. Meyer, S. Kruss, Tuning selectivity of fluorescent carbon nanotube-based neurotransmitter sensors. *Sensors (Basel)* **17**, E1521 (2017).
39. D. Meyer, A. Hagemann, S. Kruss, Kinetic requirements for spatiotemporal chemical imaging with fluorescent nanosensors. *ACS Nano* **11**, 4017–4027 (2017).
40. S. Zhang *et al.*, Dopaminergic and glutamatergic microdomains in a subset of rodent mesoaccumbens axons. *Nat. Neurosci.* **18**, 386–392 (2015).
41. M. Mani, T. A. Ryan, Live imaging of synaptic vesicle release and retrieval in dopaminergic neurons. *Front. Neural Circuits* **3**, 3 (2009).
42. C. Imig *et al.*, The morphological and molecular nature of synaptic vesicle priming at presynaptic active zones. *Neuron* **84**, 416–431 (2014).
43. F. Varoqueaux *et al.*, Total arrest of spontaneous and evoked synaptic transmission but normal synaptogenesis in the absence of Munc13-mediated vesicle priming. *Proc. Natl. Acad. Sci. U.S.A.* **99**, 9037–9042 (2002).
44. F. Varoqueaux, M. S. Sons, J. J. Plomp, N. Brose, Aberrant morphology and residual transmitter release at the Munc13-deficient mouse neuromuscular synapse. *Mol. Cell. Biol.* **25**, 5973–5984 (2005).
45. B. Cooper *et al.*, Munc13-independent vesicle priming at mouse photoreceptor ribbon synapses. *J. Neurosci.* **32**, 8040–8052 (2012).
46. J. Breustedt *et al.*, Munc13-2 differentially affects hippocampal synaptic transmission and plasticity. *Cereb. Cortex* **20**, 1109–1120 (2010).
47. H. Kawabe *et al.*, ELKS1 localizes the synaptic vesicle priming protein bMunc13-2 to a specific subset of active zones. *J. Cell Biol.* **216**, 1143–1161 (2017).
48. I. Augustin *et al.*, The cerebellum-specific Munc13 isoform Munc13-3 regulates cerebellar synaptic transmission and motor learning in mice. *J. Neurosci.* **21**, 10–17 (2001).
49. S. Ishiyama, H. Schmidt, B. H. Cooper, N. Brose, J. Eilers, Munc13-3 superprimes synaptic vesicles at granule cell-to-basket cell synapses in the mouse cerebellum. *J. Neurosci.* **34**, 14687–14696 (2014).
50. C. B. Yang, Y. T. Zheng, G. Y. Li, G. D. Mower, Identification of Munc13-3 as a candidate gene for critical-period neuroplasticity in visual cortex. *J. Neurosci.* **22**, 8614–8618 (2002).
51. Z. Chen, B. Cooper, S. Kalla, F. Varoqueaux, S. M. Young Jr., The Munc13 proteins differentially regulate readily releasable pool dynamics and calcium-dependent recovery at a central synapse. *J. Neurosci.* **33**, 8336–8351 (2013).
52. K. Tiklová *et al.*, Single-cell RNA sequencing reveals midbrain dopamine neuron diversity emerging during mouse brain development. *Nat. Commun.* **10**, 581 (2019).
53. F. Sun *et al.*, Next-generation GRAB sensors for monitoring dopaminergic activity in vivo. *Nat. Methods* **17**, 1156–1166 (2020).
54. T. Patriarchi *et al.*, An expanded palette of dopamine sensors for multiplex imaging in vivo. *Nat. Methods* **17**, 1147–1155 (2020).

55. S. J. Cragg, M. E. Rice, DAncing past the DAT at a DA synapse. *Trends Neurosci.* **27**, 270–277 (2004).
56. P.-Y. Pan, T. A. Ryan, Calbindin controls release probability in ventral tegmental area dopamine neurons. *Nat. Neurosci.* **15**, 813–815 (2012).
57. A. A. Grace, B. S. Bunney, The control of firing pattern in nigral dopamine neurons: Single spike firing. *J. Neurosci.* **4**, 2866–2876 (1984).
58. R. G. W. Staal, E. V. Mosharov, D. Sulzer, Dopamine neurons release transmitter via a flickering fusion pore. *Nat. Neurosci.* **7**, 341–346 (2004).
59. D. Sulzer, E. N. Pothos, Regulation of quantal size by presynaptic mechanisms. *Rev. Neurosci.* **11**, 159–212 (2000).
60. D. L. Cardozo, Midbrain dopaminergic neurons from postnatal rat in long-term primary culture. *Neuroscience* **56**, 409–421 (1993).
61. J. Lautenschläger, E. V. Mosharov, E. Kanter, D. Sulzer, G. S. Kaminski Schierle, An easy-to-implement protocol for preparing postnatal ventral mesencephalic cultures. *Front. Cell. Neurosci.* **12**, 44 (2018).
62. S. Rayport *et al.*, Identified postnatal mesolimbic dopamine neurons in culture: Morphology and electrophysiology. *J. Neurosci.* **12**, 4264–4280 (1992).
63. A. Burgalossi *et al.*, Analysis of neurotransmitter release mechanisms by photolysis of caged Ca^{2+} in an autaptic neuron culture system. *Nat. Protoc.* **7**, 1351–1365 (2012).
64. M. A. Cousin, J. M. Pocock, D. G. Nicholls, Intracellular free Ca^{2+} responses in electrically stimulated cerebellar granule cells. *Biochem. Soc. Trans.* **23**, 648–652 (1995).
65. R. Nißler *et al.*, Chirality enriched carbon nanotubes with tunable wrapping via corona phase exchange purification (CPEP). *Nanoscale* **11**, 11159–11166 (2019).
66. D. Sulzer, C. St Remy, S. Rayport, Reserpine inhibits amphetamine action in ventral midbrain culture. *Mol. Pharmacol.* **49**, 338–342 (1996).
67. A. H. Chouaib, AbedChouaib/FijiJava: DART v1.4 beta. Zenodo. https://zenodo.org/record/6406536#.YnwCGujMLcs. Deposited 1 April 2022.
68. M. Piccardi, "Background subtraction techniques: A review" in *2004 IEEE International Conference on Systems, Man and Cybernetics (IEEE Cat. No.04CH37583)* (IEEE, 2004), pp. 3099–3104.
69. S. Brutzer, B. Hoferlin, G. Heidemann, "Evaluation of background subtraction techniques for video surveillance" in *CVPR 2011* (IEEE) 2011), pp. 1937–1944.
70. W. G. M. Geraets, A. N. van Daatselaar, J. G. C. Verheij, An efficient filling algorithm for counting regions. *Comput. Methods Programs Biomed.* **76**, 1–11 (2004).